

# Advancing Molecular Machine (Learned) Representations with Stereoelectronics-Infused Molecular Graphs

Daniil A. Boiko,<sup>1</sup> Thiago Reschützegeger,<sup>2</sup> Benjamin Sanchez-Lengeling,<sup>3,4,5</sup> Samuel M. Blau,<sup>\*6</sup> Gabe Gomes<sup>\*1,7,8</sup>

1. Department of Chemical Engineering, Carnegie Mellon University, Pittsburgh, PA 15213, USA
2. Department of Chemical Engineering, Federal University of Santa Maria, Santa Maria, RS, Brazil
3. Google DeepMind, Cambridge, MA, USA (*previous affiliation, where most of this work was done*)
4. Department of Chemical Engineering and Applied Chemistry, University of Toronto, Toronto, ON M5S 3E5, Canada (*current affiliation*)
5. Vector Institute for Artificial Intelligence, Toronto, ON, Canada (*current affiliation*)
6. Energy Technologies Area, Lawrence Berkeley National Laboratory, Berkeley, CA 94720, USA
7. Department of Chemistry, Carnegie Mellon University, Pittsburgh, PA 15213, USA
8. Wilton E. Scott Institute for Energy Innovation, Carnegie Mellon University, Pittsburgh, PA 15213, USA

\* corresponding authors: [smblau@lbl.gov](mailto:smblau@lbl.gov), [gabegomes@cmu.edu](mailto:gabegomes@cmu.edu)

## Abstract

Molecular representation is a foundational element in our understanding of the physical world. Its importance ranges from the fundamentals of chemical reactions to the design of new therapies and materials. Previous molecular machine learning models have employed strings, fingerprints, global features, and simple molecular graphs that are inherently information-sparse representations. However, as the complexity of prediction tasks increases, the molecular representation needs to encode higher fidelity information. This work introduces a novel approach to infusing quantum-chemical-rich information into molecular graphs via stereoelectronic effects. We show that the explicit addition of stereoelectronic interactions significantly improves the performance of molecular machine learning models. Furthermore, stereoelectronics-infused representations can be learned and deployed with a tailored double graph neural network workflow, enabling its application to any downstream molecular machine learning task. Finally, we show that the learned representations allow for facile stereoelectronic evaluation of previously intractable systems, such as entire proteins, opening new avenues of molecular design.

## Keywords

Molecular machine learning, graph neural networks, molecular properties, deep learning, quantum chemistry, active learning

## Introduction

Molecular representation is a cornerstone in chemistry.<sup>1,2</sup> Following chemists' intuition, skeletal structures became the chemical *lingua franca*. They allow us to capture the wide diversity of (mostly organic) molecules, while preserving simplicity and making it

easier for humans to recognize common patterns. In addition to influencing the way chemistry is thought and described,<sup>3</sup> these representations are powering advances in molecular machine learning (ML), which has been used for various applications.

One of the most successful applications of ML in such settings is the prediction of molecular properties, which is at the core of chemical, biological, and material sciences. From the discovery of materials for solar panels<sup>4</sup> to the record-setting development of a new drug,<sup>5,6</sup> molecular ML significantly impacted modern science by enabling fast inference. The performance of the ML models is strongly connected to the underlying molecular representation, arguably the most critical factor for their success.<sup>7</sup> Current standard molecular representations encompass various approaches: global descriptors,<sup>8</sup> strings that translate the structure into a token sequence,<sup>9</sup> graphs that encode covalent bonding information,<sup>10,11</sup> providing topological information (**Figure 1a**). There are also approaches to infuse spatial information into latter representations, providing structural information.<sup>12,13</sup>

Despite the success of machine learning for molecular property predictions, the representations used in these methods are incomplete. Current graph representations lack quantum-chemical priors from the electronic structure of molecules (**Figure 1a**). Providing insight into the electronic structure of molecules, such representations as Lewis structures still focus solely on covalent bonds, neglecting delocalization and non-covalent interactions. These interactions between the corresponding bonding/nonbonding and antibonding orbitals are essential in our understanding of many chemical phenomena,<sup>14</sup> such as in protein-substrate interactions<sup>15</sup> and organocatalysis.<sup>16</sup>

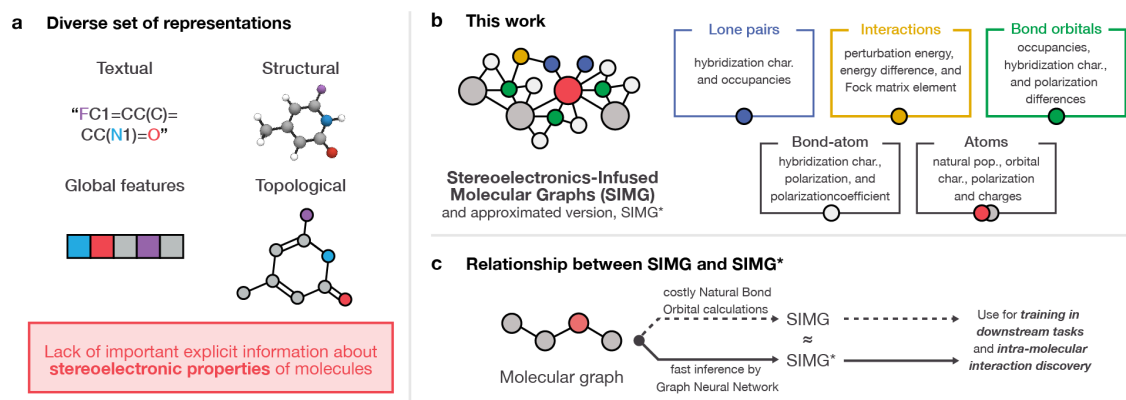


**Figure 1. Common molecular representations and overview of our approach.** **a**, Various popular molecular representations for machine learning strategies. **b**, **SIMG** construction approach. **c**, the relationship between **SIMG** and **SIMG\***.

At the same time, the computational chemistry community has developed solid foundations for describing the quantum-mechanical nature of molecular structures beyond skeletal structures. These approaches offer opportunities to increase our

understanding of chemical processes and improve ML model performance. Importantly, these approaches may be limited by the possibility of performing calculations on them.

This work introduces a new representation based on molecular graphs enhanced with nodes corresponding to bond orbitals, lone pairs, and interactions between them (which essentially encode relational 3D information), called **SIMGs** (stereoelectronics-infused molecular graphs). We describe how the **SIMG** representation (**Figure 1b**) can be constructed from Natural Bond Orbital<sup>17</sup> (NBO) analysis data and approximated with graph neural networks (**SIMG\***) to enable faster predictions (**Figure 1c**). We study how these representations can be used as input for machine learning algorithms to perform molecular property predictions and discover stereoelectronic interactions in systems where direct quantum chemical NBO calculations are intractable.

## Results

In this work, our goal is to build a new molecular machine learning representation that achieves three equally important goals: I. enhances the performance and effectiveness of predictive and generative models, especially when compared to cruder molecular graph baselines; II. rigorously based on our collective understanding that molecules are three-dimensional quantum mechanical objects that are always in motion; III. is easily human interpretable.

The work is done on two different datasets depending on the final application of the model with the third dataset released separately. To develop this representation, we start with a fully computational chemistry-based approach, constructing these new graphs from NBO calculation results. Then, we show how this representation can be approximated with separately trained graph neural networks, introducing a novel neural network module in the process.

The developed model is then applied to two distinct tasks. The first is the prediction of QM9 targets, serving as an example of downstream application where we compare our results with molecular graph and ChemProp<sup>18</sup> baselines. The second involves discovering interactions in proteins, through which we demonstrate that this approach can be extrapolated beyond the small molecules these models were initially trained on.

### 1. Stereoelectronics-Infused Molecular Graphs (**SIMGs**)

The proposed representation is based on Natural Bond Orbital analysis and a new heterogeneous graph topology. NBO analysis starts with providing a 3D structure of a given molecule and a valid description of its wave function.<sup>17</sup> NBO yields a collection of localized natural atomic orbitals, hybrid orbitals, bonding/nonbonding, and antibonding orbitals.<sup>19</sup> It does so by doing a series of transformations with the Fock-matrix<sup>20</sup> term from Hartree-Fock-derived quantum-chemistry methods,<sup>20</sup> including hybrid density functional approximations.<sup>21,22</sup> Moreover, NBO analysis quantifies interactions between filled orbitals (donors) and empty orbitals (acceptors) via second-order perturbation interactions ( $E(2)$ , in kcal mol<sup>-1</sup>). This strategy yields a quantitative description of the

quantum-mechanical nature of electronic density delocalization, rendering itself a perfect fit for heterogeneous molecular graph representations.

**SIMGs** are constructed on top of the molecule's NBO analysis data in the following way (**Figure 1b**). Differently from standard molecular graphs, which simply represent molecules as a collection of nodes for each atom and edges for each covalent bond, we propose the inclusion of new types of stereoelectronic nodes and edges. Besides the traditional atomic node, we include lone pair nodes ( $n$ ) and bond nodes ( $\sigma$ ,  $\sigma^*$ ,  $\pi$ ,  $\pi^*$ ), which represent electron density orbitals, and 2<sup>nd</sup>-order nodes, which represent interactions between electron-rich and electron-deficient orbitals, these being bond-to-bond (bonding to antibonding interaction), or lone pair-to-bond (non-bonding to antibonding interaction). Although there are works on infusing this information implicitly,<sup>23</sup> we chose an explicit approach to ease interpretability and better control the graph structure.

We can extend the topology changes from molecular graphs to **SIMGs** with numerical NBO analysis information (**Figure 1b**). In particular, Natural Population Analysis (NPA) provides information about natural atomic orbitals (NAOs). The performed NAO analysis returns localized electron information for each atom and is stored in **SIMGs** as atomic features. Atom targets include their charge, the number of core electrons, valence electrons, and total electrons.

In the context of localized natural bond orbitals, bonds are simply a combination of the hybrid orbitals from each atom. For that reason, NBO evaluation yields atom-wise  $s$ ,  $p$ ,  $d$ , and  $f$  characters, bond polarization and its coefficients, and the respective values for antibonding orbitals. Occupancy for bonding and antibonding orbitals are the only bond-specific target from the original data. In total, 26 features are assigned to bond nodes. Orbital hybridization of nonbonding orbitals (e.g., lone pairs) is described by their  $s$ ,  $p$ ,  $d$ , and  $f$  characters. Moreover, NBO analysis provides information about their occupancies, summing up to five features stored in each lone pair node.

Orbital interactions represent the electronic interactions between donor and acceptor orbitals. Donors, mostly represented by lone pairs  $n$ , as well as  $\sigma$  and  $\pi$  bonds, are electron-rich orbitals, while acceptors, represented by  $\sigma^*$  and  $\pi^*$  antibonds, are electron deficient. The ground truth graph represents one donor-acceptor interaction as a connection between the respective interacting nodes. These interactions are quantified by the 2<sup>nd</sup> order perturbation energy, energy difference, and the Fock-matrix element (three features in total).

As for the edges, we represent both atom-to-bond relationships and atom-to-atom (covalent) interactions. Atom-to-bond edges store atom-wise information about hybridization, orbital character, bond polarization and its coefficients. Atom-to-atom edges store the bond order of the corresponding covalent bond and its length. Overall, these representations show superior results over standard molecular graphs (see Section 4 for more details) while retaining ease of interpretation.

## 2. *SIMGs* surrogate with Graph Neural Networks.

Computation of required NBO data for *SIMG* construction can take significant amounts of time, severely limiting the use of such graphs over large datasets of molecular structures and conformer ensembles. Moreover, for large molecules such as proteins, these calculations are simply not feasible due to the limitations in the number of basis functions that NBO can process. The main workaround is via truncation of those macromolecules, a strategy that severely limits how we study such systems. Therefore, we aimed to develop an approach for fast prediction of *SIMG* graphs solely from molecular three-dimensional structure (e.g., Cartesian coordinates). We denote these approximated representations as *SIMG\**.

In the following sections, we discuss results over QM9 (property prediction and architecture optimization) and GEOM datasets (*evolver* module, active learning, and protein applications). Additionally, we are releasing *SIMG* graphs for the PC9 dataset. We also develop our own benchmark dataset for large molecules.

### 2.1. General approach for *SIMG\** construction

Interactions involving nonbonding orbitals are critical to molecular structure.<sup>24</sup> However, such information is absent from traditional molecular graphs, as it must be obtained from expensive quantum chemical calculations. We overcome this limitation by formulating the problem as a sequential graph construction (**Figure 2a**). As a result, the full pipeline can predict NBO interactions based on complex electronic interactions within the molecule without explicit quantum chemical calculations, as presented in **Figure 2a**.

First, the molecular graph is constructed from the three-dimensional input structure. Next, the graph is used as an input for the first model, which is responsible for predicting the number of lone pairs and their types (see full description in the “Methods” section). Once the model has successfully predicted lone pair information, we construct an intermediate graph, which we call “extended molecular graph,” that incorporates lone pair nodes and their types. For this graph, we add nodes that represent  $\sigma$ - and  $\pi$ -bonds between two atoms. With additional information contained in these nodes, this strategy is a more comprehensive way of describing connections in molecular settings, instead of simply representing covalent bonds as edges. These graphs are subsequently used as input for a second model, designed to predict electronic properties of orbital overlaps in a multitask fashion, *i.e.*, the *SIMG\** graphs.

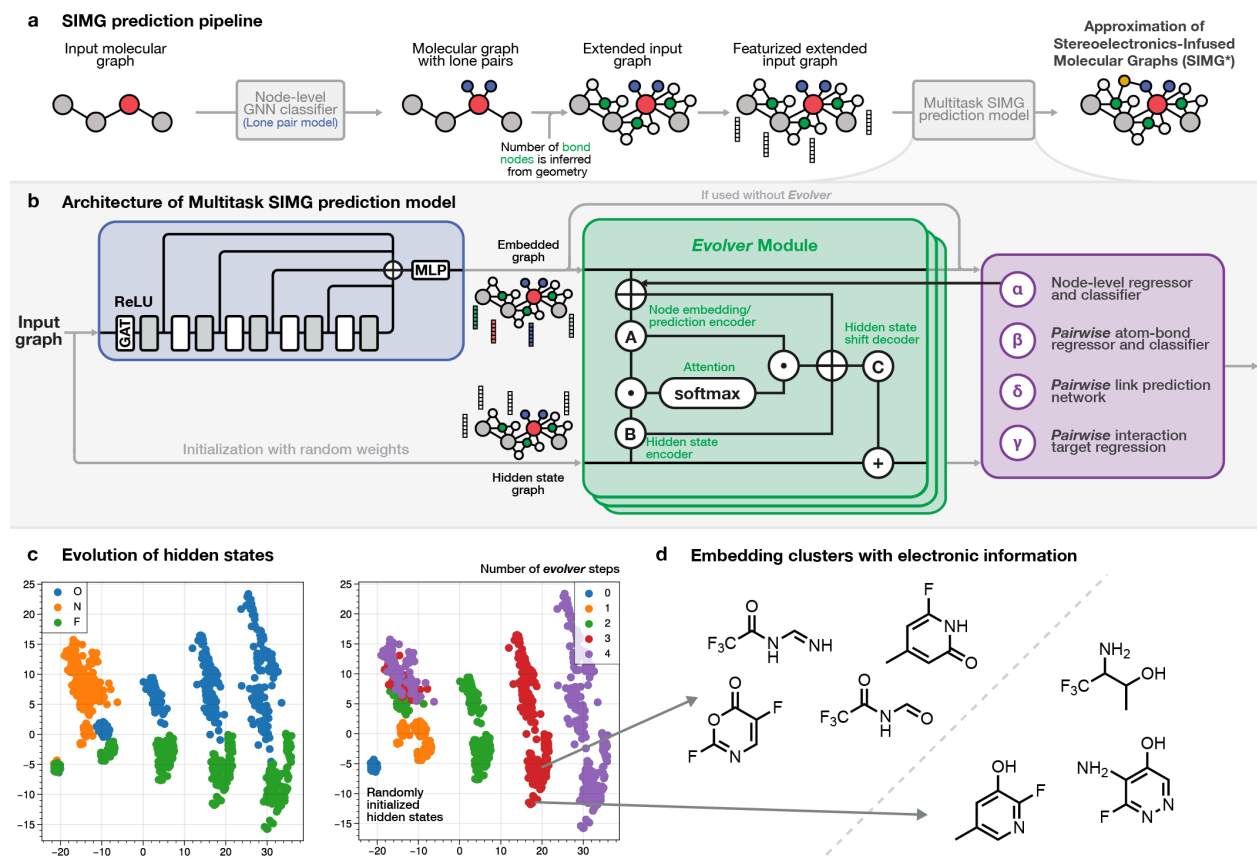


**Figure 2. Approach to *SIMG\** construction.** **a**, *SIMG\**s are constructed from molecular graphs using two models (in the example molecule, hydrogens are not shown). **b**, Architecture of the multitask model, including the *evolver* module. **c**, Evolution of the hidden states marked by atom type and step number. **d**, Two clusters of fluorine lone pairs sensing the presence of C=O bonds.

## 2.2. Architecture of the multitask model.

The multitask model takes an extended molecular graph as an input and passes it through a GNN-based encoder (**Figure 2b**).<sup>11</sup> The encoder heavily uses graph attention layers; it also includes skip-connection to address oversmoothing issues (see details in the Methods section). The output of the encoder is a set of embeddings for each of the nodes in the graph.

We employ a two-pronged approach to get *SIMG\**s from these embeddings because of the following challenge: we explicitly introduce lone pair and bond nodes that may have different targets. For example, furane — an important biological scaffold — has an oxygen atom with two lone pairs: one of them is a pure *p*-orbital that is in conjugation with the  $\pi$ -system; the other lone pair is a  $sp^A$ -hybrid completely orthogonal to the  $\pi$ -system. However, the  $sp^A$ -hybrid lone-pair can participate in the formation of hydrogen bonds and other non-covalent interactions, increasing its relevance for studying complex chemical systems. Moreover, as these nodes are added to the molecular graph later, their features are identical. For this problem, we introduce two approaches to solve it:

1. **Assign features that make it possible to differentiate these feature-identical nodes.** This is accomplished by making the lone pair model to predict mostly  $p$ - or mostly  $s$ -character of the lone pair (see the “Methods” section for more details).
2. **Introduce random hidden states and perform multiple updates of these hidden states.** Here, this is performed using five blocks of the *evolver* module (**Figure 2b**) that uses node embeddings in intermediate predictions of node targets to update these hidden states. This operation can be viewed as a learnable optimization procedure. Finally, another important piece is the development of the permutation-invariant loss function (see the “Methods section for a detailed description and Figure S2 in the Supporting Information).

Both approaches work better than the baseline model without any differentiating information (see Supporting Information, Figures S4-5 for comparison). Although the *evolver* approach is a slightly less efficient than assigning differentiating features, it is much more general and can be used for future datasets with significantly more lone pairs per atom.

The operations performed by the *evolver* module are based on iterative updates of the hidden states. Therefore, we can study how embeddings change with time steps. **Figure 2c** shows a PCA map for the node hidden states, colored by element and time step, respectively (see Figure S3 for more specific examples). It can be seen that starting at one point, the model slowly changes embeddings to spread them apart. Another observation is that elements like fluorine have two different clusters. Inspection of these clusters revealed an interesting outcome (**Figure 2d**): for fluorine, these clusters differ solely based on the presence of a C=O double bond in the molecule. However, the reasons for its importance for the model remain unclear, even though they are clearly present in the data. Finally, in comparison to vanilla GNN (see Supporting Information, Figure S9), we see a much better separation with our architecture.

### 2.3. Active learning of *SIMGs* based on epistemic uncertainty estimation

While this work shows results across multiple datasets, a primary goal was to enable predictions for a set of elements covering at least common in biological molecules (with at least all biologically relevant elements included). One of the datasets with enough chemical diversity in terms of elements, molecular size, and conformations is GEOM.<sup>25</sup> However, its immense scale makes running DFT and NBO calculations for every molecule and its conformers unreasonably costly. Instead, we decided to perform training in an active learning manner (**Figure 3a**).

The proposed methodology heavily relied on the estimation of uncertainties in the prediction of *SIMGs*. These uncertainties can be categorized into two types: aleatoric uncertainty, which arises from the inherent stochasticity of the data, and epistemic uncertainty, which stems from the presence of test objects that lie far from the points in the training dataset.<sup>26</sup> In the context of our problem, estimating epistemic uncertainty is of great importance, particularly for exploration-oriented tasks.<sup>27</sup> While there exist theoretically rigorous approaches such as Bayesian neural networks for uncertainty estimation,<sup>28</sup> these methods are notorious for their challenging training requirements.

Thus, in practical implementation, we adopted an ensemble of models and computed the variance of their predictions. This ensemble-based approach has proven to yield good results,<sup>29</sup> providing a feasible alternative to address the challenges associated with estimating epistemic uncertainty in our study.

In this work, we developed the following multistep approach. First, a uniform sample of 29,500 structures from GEOM was chosen and NBO calculations were performed. We used this data to train a lone pair prediction model and an ensemble of three multitask SIMG prediction models. Next, we performed lone pair model inference and then featurized extended input graph construction for each molecule and conformer in the GEOM dataset. We divided the dataset into 295 parts and selected 10,000 molecules from each part to pass through the models in the ensemble. For each molecule and target, we calculated the variances of the ensemble models predictions. We then selected the 1,000 molecules with the highest variances for each target, removed duplicates (as some molecules can end up in the highest variance lists of multiple targets), and submitted the new sample to NBO calculations again. As the procedure was done for every target, we ended up with 20,000–30,000 molecules each time.

The dataset modifications throughout the iterations of the active learning procedure unveiled multiple noteworthy observations, as shown in **Figure 3b** (see Figure S6 for more details). During the first iteration, the ensemble showed a preference for selecting a substantial number of molecules containing boron, which were notably underrepresented in the initial dataset. Additionally, molecules with bromine and iodine, as well as molecules containing iodine and sulfur, were chosen. In subsequent iterations, there was an increased focus on selecting molecules containing mercury and arsenic. Notably, in the final step of the active learning procedure, the ensemble collected numerous molecules with a B-Cl pair. These observed shifts in molecule selection across the iterations highlight the dynamic nature of the active learning process and emphasize the ensemble's ability to adapt and refine its selection strategy.

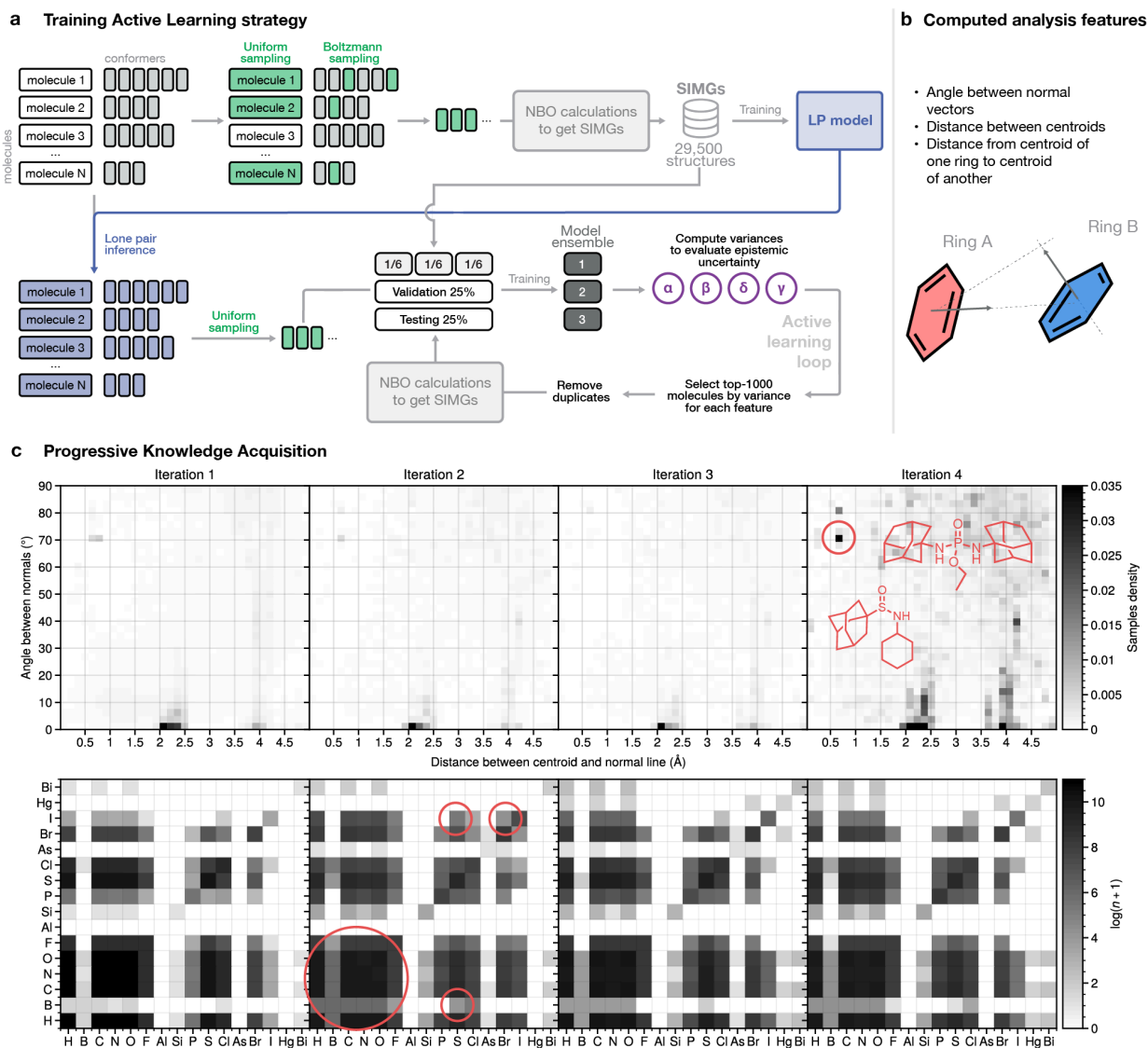


**Figure 3. Active learning approach to select data for the model. a,** Overview of the approach. **b,** Features, calculated to analyze chemical space shifts and changes of the data acquisition through iterations of the active learning procedure.

Furthermore, we conducted an analysis of the relative positions of rings within the molecule by calculating descriptors (refer to **Figure 3b**). Initially, we aimed to identify any disparities in the occurrence of molecules exhibiting  $\pi$ -stacking interactions. During the final iteration, our ensemble-based approach demonstrated a remarkable capability to selectively target numerous compounds featuring adamantane structures. This ability to discern and focus on specific subsets of compounds with elevated uncertainty showcases the approach's efficacy in effectively navigating the expansive chemical space while optimizing the exploration process.

## 2.4. Prediction performance

The findings depicted in **Figure 4** highlight the successful approximation of SIMGs utilizing graph neural networks. The model demonstrated outstanding performance in classifying the quantity and types of lone pairs at the node level, as evidenced by the confusion matrix presented in **Figure 4a**, while being able to reconstruct the ground-truth extended graph in 98% of the cases. Notably, the node-level tasks included the prediction of properties for atoms, lone pairs, and bonds. Remarkable performance was observed in atom-related tasks with excellent  $R^2$  scores achieved, with by mean absolute errors (MAEs) and root-mean-square errors (RMSEs) of less than 0.03 elementary charges. For lone pair-related tasks, particularly those involving  $s$ - and  $p$ -character, excellent predictive scores were attained. Although slightly lower scores were observed for the  $d$ -prediction task due to the limited number of  $d$ -block data points, those remained reliable. Successful predictions were also observed for lone pair occupancies. For bond-related tasks, occupancies were predicted with favorable scores. Additionally, predictions related to hybridization characters and polarizations exhibited notable accuracy with the exception for  $d$ -character, simply due to the smaller number of  $d$ -orbital containing elements in the dataset.

Some prediction targets for bonds are different for each atom, such as hybridization characters and polarizations, and polarization coefficients. These were predicted with a separate network, which used the corresponding node embedding as an input. As a result, exceptional performance was achieved for all targets except  $d$ -characters for the previously discussed reasons.

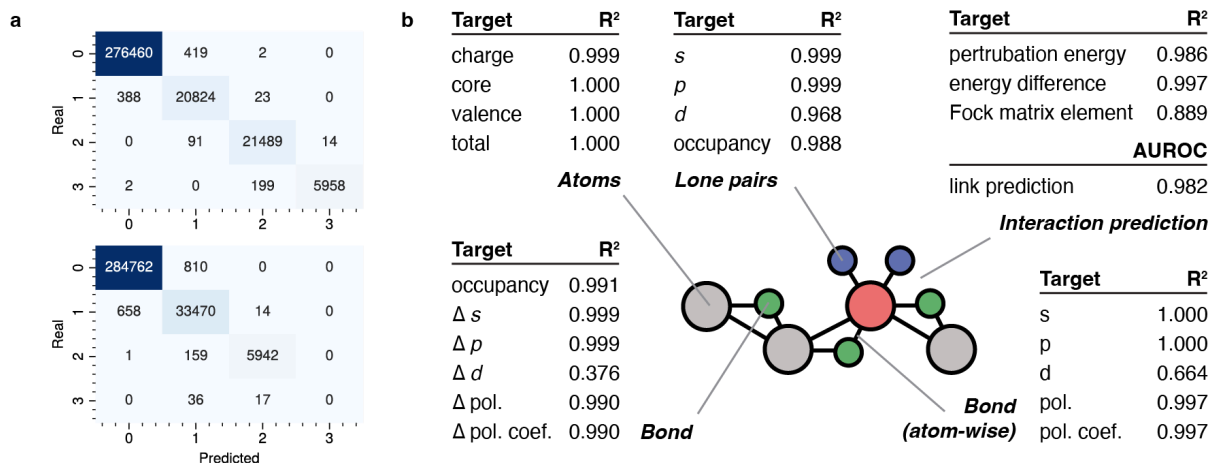


**Figure 4. Quality of SIMG\* predictions.** **a**, Confusion matrix for lone pair count, and type prediction, respectively. **b**, Prediction performance for the second model.

Prediction of second-order interactions ( $E(2)$ ) can be cast as a classic link prediction problem. As this is a classification problem, we used AUROC (area under the receiver operating characteristic curve) and mean AUROC. The value of AUROC is equal to 0.982, which is a good result for such complex tasks. The value for the mean AUROC of 0.979 is slightly smaller. Finally, the properties of these interactions were also predicted;

the only decline in performance is observed for the values of Fock matrix elements (**Figure 4b**).

### 3. *SIMG*\*s enable predictions for previously inaccessible molecules.

Stereoelectronic interactions, as derived from NBO data and subsequently obtained through *SIMG*s, assume a crucial role in the stability of large molecules.<sup>30-32</sup> Notably, spatial structures of proteins primarily rely on the presence of hydrogen bonds for stability. Additionally, an array of weaker interactions collectively contributes significantly to the overall stabilization energy. Unfortunately, even with the most recent version of the NBO program, computations are limited to molecules containing up to 999 atoms, rendering them infeasible for larger molecules. However, owing to the localized nature of stereoelectronic effects, encompassing both bond distances within the molecule and spatial distances, it becomes feasible to gain insights into these interactions through the study of much smaller molecules, such as those within the GEOM dataset.

To assess the model's effectiveness in identifying particular structural features within large molecules, particularly proteins, we focused on a subset of the Potassium Channel KcsA-Fab complex in a low concentration of  $K^+$  (PDB code 1k4d).<sup>33</sup> The specific structures of interest were the interactions in an  $\alpha$ -helix involving the  $p$ -rich lone pair electrons of the amide oxygen atom ( $n_o$ ) and the antibonding  $\pi$ -orbital of the adjacent carbonyl group ( $\pi_{CO}^*$ ), as shown in **Figure 5d**. Such  $n_o \rightarrow \pi_{CO}^*$  interactions were previously reported in this protein and were predicted through NBO analysis, serving as a basis for our evaluation.<sup>34</sup>

In the context of the entire protein structure, we built Ramachandran plots as presented in **Figure 5a**. Specifically, we focused on identifying the dihedral angles associated with selected subgraphs where the potential presence of  $n_o \rightarrow \pi_{CO}^*$  interactions could occur. These dihedral angles are defined by  $\phi(C'_{i-1}-N_i-C^\alpha_i-C'_i)$  and  $\Psi(N_i-C^\alpha_i-C'_i-N_{i+1})$ . Our model successfully predicted the aforementioned interactions in most instances, as depicted in **Figure 5a**. Finally, model predictions of  $E(2)$  second-order interaction are closely related to its ground truth (**Figure 5c**).

Furthermore, our research aimed to assess the model's performance in capturing and comprehending long-range interactions, encompassing both graph-based structural relationships and physical distances. To achieve this, we quantified the predicted interactions and performed a comparative analysis with ground-truth NBO calculations. To ensure unbiased measurements, we utilized the F1-score as it is a suitable metric for evaluating imbalanced classifications, as shown in **Figure 5b**. Observations highlighted a positive correlation between the model's performance and the abundance of interaction samples. It was interesting to note that when the distance between atoms was below 2.8 Å and the graph distance was under 4, there was a substantial increase in the number of existing interactions. This trend contributed to the model's enhanced performance in predicting interactions within these ranges. Critically, we note that the

available training data with instances of longer-range interactions (atom distances >2.8 Å, graph distances >4) is scarce.

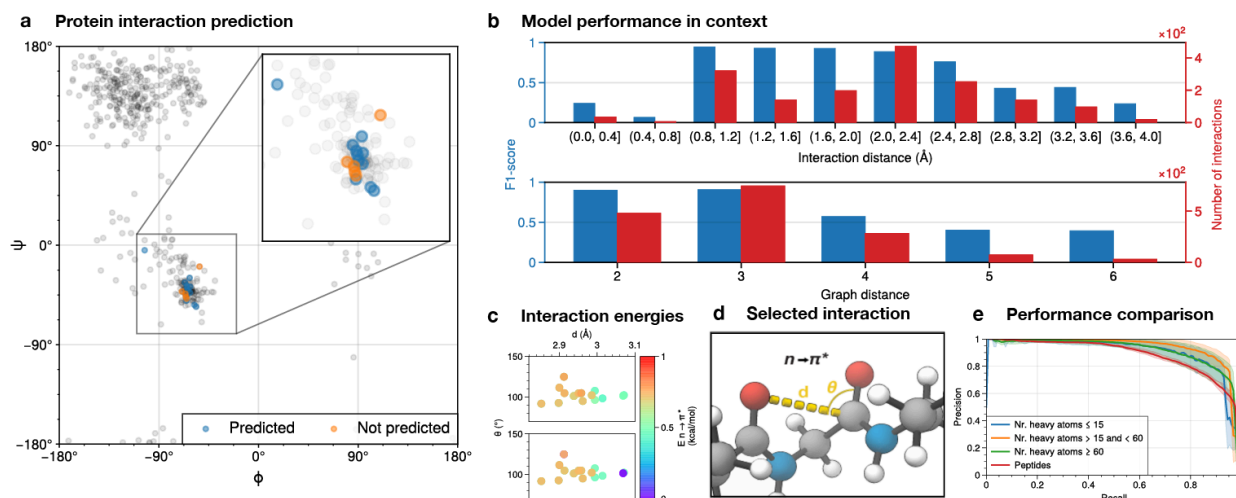


**Figure 5. Assessment of Model Performance in Identifying Structural Features and Long-Range Interactions in Proteins.** **a**, Ramachandran plot illustrating the identification of structural features, specifically the selected subgraphs and associated dihedral angles ( $\phi$  and  $\Psi$ ) related to potential  $n_o \rightarrow \pi_{CO}^*$  interactions in the  $\alpha$ -helix of the Potassium Channel KcsA-Fab complex. **b**, Model performance evaluation for capturing long-range interactions using the F1-score metric. (Graph distance histogram was truncated for better readability). **c**, Strong correlation between predicted and actual energy values associated with the identified interactions. **d**, Visualization of a  $n_o \rightarrow \pi_{CO}^*$  contact within the  $\alpha$ -helix structure, supported by previous reports and NBO analyses. **e**, Precision-Recall curves comparing the performance of the model for molecules of varying sizes, from small molecules to peptides.

To see how well our models perform for large systems, we created an additional set of large molecules (primarily neutral, closed-shell, truncated peptides approaching the limit of computational feasibility with the quantum chemistry methodologies employed in this work) and performed NBO calculations on them to get **SIMGs**. These **SIMGs** were then compared with predicted **SIMGs**\*. **Figure 5** shows that the model successfully captures the stereoelectronic interactions without significant differences in performance when compared with smaller molecules. Moreover, the only significant difference between a large molecule and an example from the GEOM dataset is bond distance (*i.e.*, distance in the graph), not observable spatial distance. We compared the model's performance for cases with various graph distances calculated with the Dijkstra algorithm and have not observed any correlation between them. Aggregated metrics also reveal no significant difference (**Figure 5e**).

#### 4. **SIMG** and **SIMG**\* as efficient representations in downstream molecular machine learning tasks

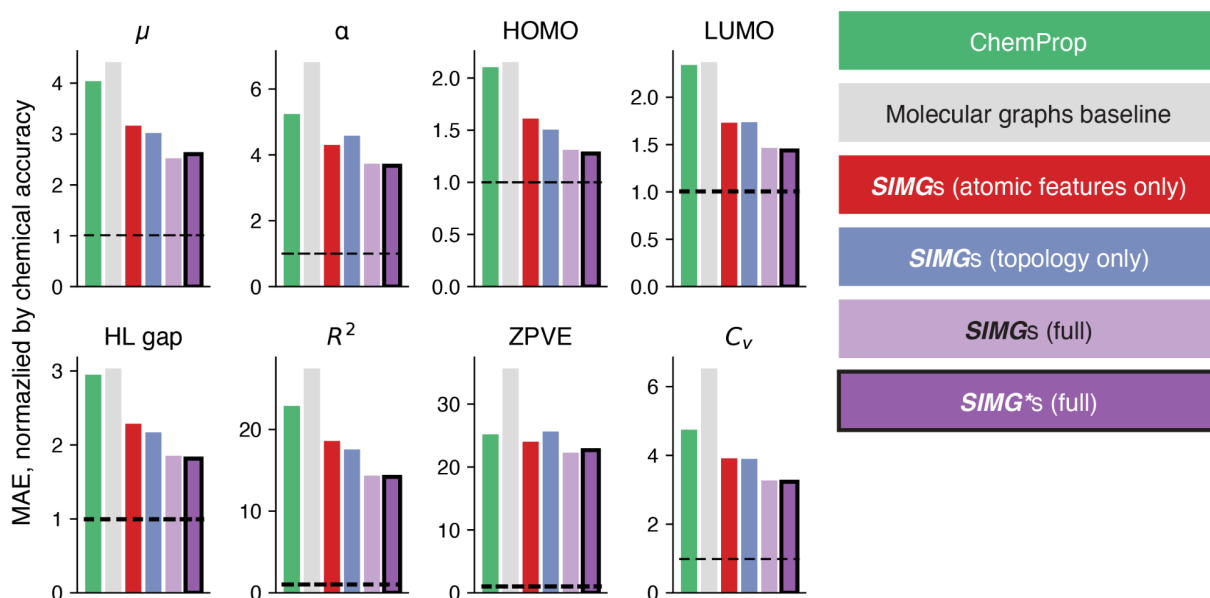


**Figure 6.** Comparison of **SIMG** and **SIMG\*** (with and without features/graph topology) with baselines on property prediction tasks. Metrics (mean absolute error, MAE; lower is better) are normalized by chemical accuracy. Each subplot represents one of the targets from QM9 dataset, bar chart elements correspond to our models and baselines. The horizontal dashed line indicates chemical accuracy.

In the final stage of this investigation, our focus shifted towards evaluating the representation's efficacy in downstream tasks. Specifically, we assessed the influence of graph augmentation by comparing three distinct graph structures: *i*) molecular graphs with additional features as done in ChemProp (default hyperparameters);<sup>18</sup> *ii*) standard molecular graphs; *iii*) **SIMGs** having original molecular graph topology but extended atom feature set; and *iv*) **SIMGs** incorporating topological structure without adding new features; *v*) complete **SIMGs**. Through this comparative analysis, we were able to distinguish effects caused by the incorporation of additional features and changing graph topology. Furthermore, the evaluation was conducted utilizing both ground-truth **SIMGs** and their learned counterparts generated by our model, denoted as **SIMG\*s** (*vi*).

For predicting downstream property-prediction tasks at the molecular (or graph) level, we selected the QM9 dataset. It comprises a wide variety of molecular structures accompanied by quantum mechanical properties. **Figure 6** shows the performance of the different graphs using the same model architecture. As one can see, **SIMGs** with atomic features and topology provide a comparable improvement to both the molecular graph and ChemProp baselines (with the exception of ZPVE for the latter). Combining both results in even bigger improvement, especially for tasks such as dipole moment prediction. Finally, the learned representation **SIMG\*** displays virtually the same results as the original **SIMGs**, but orders of magnitude faster (~10 s per molecule with all the preprocessing steps against tens of hours for large molecules). Moreover, in terms of absolute values for many targets such as  $\mu$  and HL gap, our learned representation brings corresponding models much closer to the chemical accuracy target.

The provided results confirm a significant improvement in performance of the models using the developed representation. We believe that **SIMG**\*s can readily be employed as an input to improve other molecular ML models and tasks, including protein folding and equivariant graph neural network interatomic potentials.

## Discussion

This work proposed stereoelectronics-infused molecular graphs (**SIMGs**): a new type of molecular machine learning representation that incorporates quantum-chemical interactions beyond classic Lewis structures. While preserving interpretability, **SIMGs** dramatically increase performance in downstream ML applications, such as property predictions. Moreover, we described how these representations could be approximated with graph neural networks, yielding **SIMG**\*s. In the first step, molecular graphs are extended with bond nodes and lone pair nodes, the number of which is computed by a graph neural network. The extended graphs are then used as input for another model, which solves multitask NBO analysis data prediction problem (node-level and link prediction tasks). This model uses the **evolver** module to perform multistep optimization of the hidden states of individual nodes. Finally, the extended graphs are enriched with features that can be used to represent various downstream tasks, including prediction of molecular properties and analysis of interactions in proteins.

### Model limitation and recommendations

In our representations, elements are one-hot encoded, so to add another element, one needs to collect an extended dataset of NBO analysis data, including the new element. This could be circumvented by using the physical properties of elements as features, but it requires further research.

### Broader impacts

Molecular machine learning is a critical component of pipelines for drug and material discovery, catalyst optimization, and a valuable tool for studying complex biochemical processes. Infusion of electronic data into graph representations for molecular ML will increase trust in these algorithms, contribute to increased interpretability of the models, and open new opportunities to research the relationship between electronic structure and molecular properties. Moreover, this work can also be used for the theoretical chemistry community once it allows high-throughput NBO analysis. The predicted orbitals can be applied to analyze chemical reactivity in a wide range of systems.<sup>35–38</sup>

# Methods

## 1. Data collection

Given the optimized structures for each molecule of the QM9 dataset,<sup>39</sup> we conducted single-point calculations at the  $\omega$ B97M-V<sup>40</sup>/def2-SVPD+ level of theory.

We used Q-Chem 6.0.1<sup>41</sup> interfaced with NBO 7.0<sup>42</sup> and performed the calculations via the high-throughput workflow infrastructure implemented in the Materials Project open-source software codes Pymatgen,<sup>43</sup> Custodian,<sup>44</sup> and Atomate,<sup>45</sup> resulting in targets for atom, bond, lone pairs, and orbital interactions, illustrated in **Figure 1b**. These are described as follows:

**Atom features.** The performed natural atomic orbital analysis returns localized electron information for each atom. Atom targets include their charge, the number of core electrons, valence electrons, and total electrons. Even though NBO analysis provides Rydberg orbitals, we did not keep them as a model's target due to the controversy in the physical meaning.

**Bond features.** In the context of localized natural bond orbitals, bonds are simply a combination of the orbitals from each atom. For that reason, the NBO analysis data provides atom-wise *s*, *p*, *d*, and *f* characters, polarization, polarization coefficient, and the respective values for antibonding orbitals. Occupancy for bonding and antibonding orbitals are the only bond-specific target from the original data. In total, there are a total of twenty-six targets.

**Lone pair features.** Orbital hybridization is described by the *s*, *p*, *d*, and *f* characters. Also, the NBO analysis provides information about its occupancy, summing up to five targets.

**Orbital (2<sup>nd</sup>-order) interactions.** These represent the interactions between donor and acceptor orbitals. Donors, represented by lone pairs *n*,  $\sigma$ , and  $\pi$  bonds, are electron-rich orbitals, while acceptors, represented by  $\sigma^*$ , and  $\pi^*$  anti-bonds are electron deficient. In practical terms, our ground truth graph represents one donor-acceptor interaction as a connection between the respective nodes. The NBO analysis quantified these interactions by the perturbation energy, energy difference, and the Fock-matrix element, with a total of three targets.

## 2. Model implementation and training

All models were implemented using PyTorch framework.<sup>46</sup> Model training and metric collection was implemented using PyTorch Lightning framework.<sup>47</sup> PyTorch Geometric was used for graph neural networks.<sup>48</sup> Code is available at <https://github.com/gomesgroup/simg>.

### 3. Lone pair prediction

**Tasks.** Although many heuristics can be used to define the number of lone pairs, we argue that a data-driven model is more well-suited in this case since it can interpolate between different contexts. With this in mind, we built a neural network capable of predicting each atom's number of lone pairs and their types. Such types were used to distinguish lone pairs of the same atom, since there are possible differences in their NBO data. Therefore, we determined the types by an analytical threshold relating *s*- and *p*-characters, expressing the conjugation likelihood of a given lone pair. The threshold is defined by the inequality below:

$$p_{character} - s_{character} > 80$$

Indeed, this relationship expresses the conjugation likelihood of a lone pair. In that sense, we train the neural network to predict how many lone pairs satisfy the threshold.

**Graph encoder.** Both tasks were tackled in tandem with a mapping function modeled as a GNN. To mitigate the over-smoothing problem, we used multiple aggregation functions through the message-passing scheme,<sup>49</sup> along with residual connections.<sup>50,51</sup> The encoder is constructed by stacking several propagation layers followed by a ReLU activation function. Node embeddings are then concatenated with a residual connection from the input graph. Finally, the result is forwarded to a multilayer perceptron (MLP), which, in this case, is composed of two linear layers separated by a ReLU activation layer.

**Training.** As a design choice, we framed both tasks as node-level classification issues, in which each class represents the number of lone pairs and how many satisfy the threshold, respectively. Therefore, we used the sum of the cross-entropy loss of each task as the loss function.

## 4. Property and interaction prediction model

### 4.1. General remarks

The neural network architecture comprises two parts: the node encoder and a group of multiple separate MLPs. The latter make predictions using the embeddings from the encoder part, but multiple preprocessing steps may be conducted depending on the task.

The encoder is constructed by stacking multiple graph neural network blocks and concatenating the outputs of each block. A block comprises a graph attention layer and a ReLU activation layer.<sup>52</sup> None of the dropout or batch normalization layers was used. Concatenated outputs were then passed into the MLP network with one single layer to construct the node embedding.

This encoder architecture is designed to tackle the over-smoothing issues of graph neural networks.<sup>53</sup> The problem arises when multiple graph neural network layers are stacked, making the computational graphs nearly identical. Over-smoothing might not

be a severe issue for graph-level tasks, but it is a significant issue in performing node-level tasks. There is a wide variety of approaches to solve it.<sup>50,51</sup> In this work, we concatenate outputs of intermediate layers tackling both the over-smoothing and vanishing gradients difficulties.

All MLPs for separate tasks follow the same architecture: one linear layer, the ReLU activation, the batch normalization layer, and one final linear layer. The following sections describe input preparation and loss functions for these networks.

$$L = L_{\alpha} + L_{\beta} + L_{\gamma} + L_{\delta}$$

**Atom, lone pair, and bond nodes.** The most straightforward difficulty to solve is the prediction of targets for individual nodes. Here, for all types of nodes, only one network is used. The loss function was defined as a sum of separate losses for each node type. The mean squared error (MSE) loss was used for all features except orbital characters of lone pairs. Orbital character prediction was optimized with a cross-entropy loss function. MSE was also the key metric for this type of task.  $R^2$  scores were also recorded.

$$L_{\alpha} = MSE(\alpha(x), y) + BCE(\alpha(x), y)$$

**Atom-wise bond target prediction.** Some bond features are related to each of the atoms. To keep permutation invariance, it was impossible to predict them in the previous step. The task was solved by concatenating embeddings of the atom in question and the corresponding bond, and then passing it into the MLP. Polarization value prediction was optimized with MSE loss. Orbital characters were optimized with cross-entropy loss. Similar to the previous section, MSE and the  $R^2$  score were used to control the training.

$$L_{\beta} = MSE(\beta(x), y) + BCE(\beta(x), y)$$

**Link prediction approach.** Orbital interactions data is not available directly from the molecular structure, so it should be predicted first. Therefore, the problem was formulated as a link prediction task, essentially a classification problem. “Positive examples” (i.e., cases where there is an interaction) were taken from the original dataset, while “negative examples” were sampled from other possible combinations of bonds and lone pairs. Moreover, the direction is essential as (in our case) it describes the donor-acceptor pair but not vice versa. Input data consisted of concatenated embeddings of corresponding nodes and dynamically calculated pairwise features. We performed the training with binary cross-entropy loss. Standard classification metrics were calculated for accuracy, precision, recall, F1-score, and area under the receiver operating characteristic curve (ROC AUC).

$$L_{\gamma} = BCE(\gamma(x), y) = \sum_{i,j}^n -y \log \log (\gamma(x_i, x_j, p_{i,j})) - (1 - y) \log \log (1 - \gamma(x_i, x_j, p_{i,j}))$$

**Interaction edge target prediction.** Predicted interactions can then be used as input to the network for interaction target prediction. The features were obtained by concatenating node embeddings and dynamically calculated pairwise features. Finally, we trained the network with MSE loss.

$$L_{\delta} = \text{MSE}(\delta(x), y)$$

#### 4.2. *evolver* module

The problem of having different targets for nodes with identical features can be solved by enforcing the permutation invariance in the loss function and letting the model make different predictions given identical features. The first part can be addressed by matching the model's predictions and target values. The second part can be solved by infusing randomness into the model (e.g., by randomly initializing hidden states for each node).

To compute the loss function value, we need to find a permutation with the lowest value of the loss function. Considering all possible permutations – even within one molecule – is completely unfeasible ( $O(n!)$  time complexity, where  $n$  is the number of nodes). To do that more efficiently, only lone pairs were selected. Then, within each group of lone pairs of a particular atom, a Hungarian algorithm was run to minimize the total loss function value for this group of nodes. This yields  $O(gm^3)$  time complexity, where  $g$  is the number of groups and  $m$  is the number of nodes in the group). It is important to note, that  $m$  is usually small: from 2 to 3 for the QM9 dataset, which makes the overall approach highly efficient. Finally, the corrected node order is used to compute final predictions (including predictions for pairwise tasks). This procedure is performed at each training step of the neural network.

All final predictions for the NBO model are based on the embeddings obtained from the graph neural network encoder. To infuse randomness, the most straightforward strategy is to initialize randomly sampled hidden states and then concatenate them with GNN embeddings to make final predictions. However, in such a setting, there is a chance that these embeddings will be similar enough to result in identical predictions. To solve that, we need to make the model aware of the existence of other nodes.

These ideas are reflected in the architecture of the *evolver* module (**Figure 2b**). First, concatenated node embeddings and hidden states are used to make node-level predictions. These predictions are then passed into the module along with corresponding hidden states. Then they are transformed into intermediate representations using multilayer fully connected networks (*A* and *B*, respectively). Representations of node embeddings and hidden states are then used to compute the dot product and corresponding weighting coefficients using a *softmax* function. These weights are then used to calculate new vectors, concatenated, and passed through another multilayer fully connected decoding network (*C*). Finally, the decoded representation is added to the previous hidden states. The procedure is performed multiple times.

## Acknowledgments

The authors thank NSF ACCESS (project no. CHE220012), Google Cloud Platform, NVIDIA Academic Hardware Grant Program (project titled “New molecular graph representations in joint feature spaces”) for computational resources. G.G. and D.B. acknowledge the financial support by the National Science Foundation Center for Computer-Assisted Synthesis (Grant no. 2202693) and a supporting seed grant from X, the moonshot factory (an Alphabet company). G.G. thanks CMU and the departments of chemistry and chemical engineering for the startup support. G.G. thanks Prof. Frank Weinhold (UW Madison) for the development of NBO and the many discussions about the theory and software.

S.M.B. acknowledges financial support by the Laboratory Directed Research and Development Program of Lawrence Berkeley National Laboratory under U.S. Department of Energy Contract No. DE-AC02-05CH11231. Computational resources for the high-throughput virtual screening and datasets development were provided by the National Energy Research Scientific Computing Center (NERSC), a U.S. Department of Energy Office of Science User Facility under Contract No. DE-AC02-05CH11231, and by the Lawrence Livermore computational cluster resource provided by the IT Division at the Lawrence Berkeley National Laboratory (Supported by the Director, Office of Science, Office of Basic Energy Sciences, of the U.S. Department of Energy under Contract No. DE-AC02-05CH11231).

We thank Prof. John Kitchin (CMU Chemical Engineering) and Prof. Olexandr Isayev (CMU Chemistry) for their constructive feedback.

Any opinions, findings, and conclusions or recommendations expressed in this material are those of the author(s) and do not necessarily reflect the views of the National Science Foundation, the U.S. Department of Energy, Alphabet (and its subsidiaries), or any of the other funding sources.

## Code and data availability

The code will be available at <https://github.com/gomesgroup/simg>. The data and model weights are available at <https://huggingface.co/gomesgroup/simg>.

## Author contributions

D.A.B. designed the computational pipeline and implemented **SIMG\*** prediction, active learning process, downstream task analysis and the first version of large molecule analysis. T.R. implemented the lone pair prediction model and performed analysis of large molecule predictions. B.S.-L. advised on the development of machine learning pipeline and software development. S.M.B. performed quantum chemistry calculations and advised on analysis of NBO data. G.G. designed the concept and performed preliminary studies. S.M.B. and G.G. supervised the project. D.A.B, T.R., and G.G. wrote this manuscript with input from all authors.

## References

1. Hoffmann, R. & Laszlo, P. Representation in Chemistry. *Angew Chem Int Ed Engl* **30**, 1–16 (1991).
2. Cooke, H. A historical study of structures for communication of organic chemistry information prior to 1950. *Org Biomol Chem* **2**, 3179 (2004).
3. Springer, M. T. Improving Students' Understanding of Molecular Structure through Broad-Based Use of Computer Models in the Undergraduate Organic Chemistry Lecture. *J Chem Educ* **91**, 1162–1168 (2014).
4. Gómez-Bombarelli, R. *et al.* Design of efficient molecular organic light-emitting diodes by a high-throughput virtual screening and experimental approach. *Nat Mater* **15**, 1120–1127 (2016).
5. Zhavoronkov, A. *et al.* Deep learning enables rapid identification of potent DDR1 kinase inhibitors. *Nat Biotechnol* **37**, 1038–1040 (2019).
6. Dara, S., Dhamercherla, S., Jadav, S. S., Babu, C. M. & Ahsan, M. J. Machine Learning in Drug Discovery: A Review. *Artif Intell Rev* **55**, 1947–1999 (2022).
7. Gallegos, L. C., Luchini, G., St. John, P. C., Kim, S. & Paton, R. S. Importance of Engineered and Learned Molecular Representations in Predicting Organic Reactivity, Selectivity, and Chemical Properties. *Acc Chem Res* **54**, 827–836 (2021).
8. Sandfort, F., Strieth-Kalthoff, F., Kühnemund, M., Beecks, C. & Glorius, F. A Structure-Based Platform for Predicting Chemical Reactivity. *Chem* **6**, 1379–1390 (2020).
9. Ross, J. *et al.* Large-scale chemical language representations capture molecular structure and properties. *Nat Mach Intell* **4**, 1256–1264 (2022).
10. Yang, Z., Chakraborty, M. & White, A. D. Predicting chemical shifts with graph neural networks. *Chem Sci* **12**, 10802–10809 (2021).
11. Zhou, J. *et al.* Graph neural networks: A review of methods and applications. *AI Open* **1**, 57–81 (2020).
12. Fang, X. *et al.* Geometry-enhanced molecular representation learning for property prediction. *Nat Mach Intell* **4**, 127–134 (2022).
13. Batzner, S. *et al.* E(3)-equivariant graph neural networks for data-efficient and accurate interatomic potentials. *Nat Commun* **13**, 2453 (2022).
14. Černý, J. & Hobza, P. Non-covalent interactions in biomacromolecules. *Physical Chemistry Chemical Physics* **9**, 5291 (2007).

15. Anighoro, A. Underappreciated Chemical Interactions in Protein–Ligand Complexes. in *Quantum Mechanics in Drug Discovery*, 75–86 (2020). doi:10.1007/978-1-0716-0282-9\_5.
16. Wheeler, S. E., Seguin, T. J., Guan, Y. & Doney, A. C. Noncovalent Interactions in Organocatalysis and the Prospect of Computational Catalyst Design. *Acc Chem Res* **49**, 1061–1069 (2016).
17. WEINHOLD, F. & LANDIS, C. R. NATURAL BOND ORBITALS AND EXTENSIONS OF LOCALIZED BONDING CONCEPTS. *Chem Educ Res Pract* **2**, 91–104 (2001).
18. Heid, E. *et al.* Chemprop: A Machine Learning Package for Chemical Property Prediction. *J Chem Inf Model* **64**, 9–17 (2024).
19. Alabugin, I. V. *Stereoelectronic Effects: A Bridge Between Structure and Reactivity*. (John Wiley & Sons, 2016).
20. Echenique, P. & Alonso, J. L. A mathematical and computational review of Hartree–Fock SCF methods in quantum chemistry. *Mol Phys* **105**, 3057–3098 (2007).
21. Burke, K. & Wagner, L. O. DFT in a nutshell. *Int J Quantum Chem* **113**, 96–101 (2013).
22. Goerigk, L. & Grimme, S. Double-hybrid density functionals. *Wiley Interdiscip Rev Comput Mol Sci* **4**, 576–600 (2014).
23. Kneiding, H. *et al.* Deep Learning Metal Complex Properties with Natural Quantum Graphs. *Chem Sci* **2**, 618–633 (2022).
24. Johnson, E. R. *et al.* Revealing Noncovalent Interactions. *J Am Chem Soc* **132**, 6498–6506 (2010).
25. Axelrod, S. & Gómez-Bombarelli, R. GEOM, energy-annotated molecular conformations for property prediction and molecular generation. *Sci Data* **9**, 185 (2022).
26. Malinin, A., Prokhorenkova, L. & Ustimenko, A. Uncertainty in Gradient Boosting via Ensembles. 1–17 (2020). arXiv:2006.10562
27. Chua, K., Calandra, R., McAllister, R. & Levine, S. Deep Reinforcement Learning in a Handful of Trials using Probabilistic Dynamics Models. (2018). arXiv:1805.12114
28. Goan, E. & Fookes, C. Bayesian Neural Networks: An Introduction and Survey. in *Case Studies in Applied Bayesian Data Science* (2020) doi:10.1007/978-3-030-42553-1\_3.
29. Beluch, W. H., Genewein, T., Nurnberger, A. & Kohler, J. M. The Power of Ensembles for Active Learning in Image Classification. in *2018 IEEE/CVF Conference on Computer Vision and Pattern Recognition* 9368–9377 (IEEE, 2018). doi:10.1109/CVPR.2018.00976.

30. León, I., Alonso, E. R., Cabezas, C., Mata, S. & Alonso, J. L. Unveiling the  $n \rightarrow \pi^*$  interactions in dipeptides. *Commun Chem* **2**, 3 (2019).
31. Newberry, R. W., Bartlett, G. J., VanVeller, B., Woolfson, D. N. & Raines, R. T. Signatures of  $n \rightarrow \pi^*$  interactions in proteins. *Protein Science* **23**, 284–288 (2014).
32. Hodges, J. A. & Raines, R. T. Energetics of an  $n \rightarrow \pi^*$  Interaction that Impacts Protein Structure. *Org Lett* **8**, 4695–4697 (2006).
33. Zhou, Y., Morais-Cabral, J. H., Kaufman, A. & MacKinnon, R. Chemistry of ion coordination and hydration revealed by a  $K^+$  channel–Fab complex at 2.0 Å resolution. *Nature* **414**, 43–48 (2001).
34. Bartlett, G. J., Choudhary, A., Raines, R. T. & Woolfson, D. N.  $n \rightarrow \pi^*$  interactions in proteins. *Nat Chem Biol* **6**, 615–620 (2010).
35. dos Passos Gomes, G. & Alabugin, I. V. Drawing Catalytic Power from Charge Separation: Stereoelectronic and Zwitterionic Assistance in the Au(I)-Catalyzed Bergman Cyclization. *J Am Chem Soc* **139**, 3406–3416 (2017).
36. Gomes, G. dos P., Vil', V., Terent'ev, A. & Alabugin, I. V. Stereoelectronic source of the anomalous stability of bis-peroxides. *Chem Sci* **6**, 6783–6791 (2015).
37. Grabowski, S. J. Tetrel bond– $\sigma$ -hole bond as a preliminary stage of the  $S_N2$  reaction. *Phys. Chem. Chem. Phys.* **16**, 1824–1834 (2014).
38. Sarazin, Y., Liu, B., Roisnel, T., Maron, L. & Carpentier, J.-F. Discrete, Solvent-Free Alkaline-Earth Metal Cations: Metal···Fluorine Interactions and ROP Catalytic Activity. *J Am Chem Soc* **133**, 9069–9087 (2011).
39. Ramakrishnan, R., Dral, P. O., Rupp, M. & von Lilienfeld, O. A. Quantum chemistry structures and properties of 134 kilo molecules. *Sci Data* **1**, 140022 (2014).
40. Mardirossian, N. & Head-Gordon, M.  $\omega$ B97M-V: A combinatorially optimized, range-separated hybrid, meta-GGA density functional with VV10 nonlocal correlation. *J Chem Phys* **144**, 214110 (2016).
41. Shao, Y. *et al.* Advances in molecular quantum chemistry contained in the Q-Chem 4 program package. *Mol Phys* **113**, 184–215 (2015).
42. Glendening, E. D., Landis, C. R. & Weinhold, F. *NBO 7.0*: New vistas in localized and delocalized chemical bonding theory. *J Comput Chem* jcc.25873 (2019) doi:10.1002/jcc.25873.
43. Ong, S. P. *et al.* Python Materials Genomics (pymatgen): A robust, open-source python library for materials analysis. *Comput Mater Sci* **68**, 314–319 (2013).

44. Blau, S., Spotte-Smith, E. W. C., Wood, B., Dwaraknath, S. & Persson, K. Accurate, Automated Density Functional Theory for Complex Molecules Using On-the-fly Error Correction. *ChemRxiv* (2020). doi: 10.26434/chemrxiv.13076030.v1
45. Mathew, K. *et al.* Atomate: A high-level interface to generate, execute, and analyze computational materials science workflows. *Comput Mater Sci* **139**, 140–152 (2017).
46. Paszke, A. *et al.* PyTorch: An Imperative Style, High-Performance Deep Learning Library. in *Advances in Neural Information Processing Systems 32* (eds. Wallach, H. *et al.*) 8024–8035 (Curran Associates, Inc., 2019).
47. Falcon, W. A., *et al.* PyTorch Lightning. *GitHub*. Note: <https://github.com/PyTorchLightning/pytorch-lightning> (2019).
48. Fey, M. & Lenssen, J. E. Fast Graph Representation Learning with PyTorch Geometric. (2019). arXiv:1903.02428
49. Corso, G., Cavalleri, L., Beaini, D., Liò, P. & Veličković, P. Principal Neighbourhood Aggregation for Graph Nets. (2020). arXiv:2004.05718
50. Li, G., Müller, M., Thabet, A. & Ghanem, B. DeepGCNs: Can GCNs Go as Deep as CNNs? (2019). arXiv:1904.03751
51. Godwin, J. *et al.* Simple GNN Regularisation for 3D Molecular Property Prediction & Beyond. (2021). arXiv:2106.07971
52. Veličković, P. *et al.* Graph Attention Networks. (2017). arXiv:1710.10903
53. Cai, C. & Wang, Y. A Note on Over-Smoothing for Graph Neural Networks. (2020). arXiv:2006.13318

Supporting information for the article

# Advancing Molecular Machine (Learned) Representations with Stereoelectronics-Infused Molecular Graphs

by

Daniil A. Boiko,<sup>1</sup> Thiago Reschützegeger,<sup>2</sup> Benjamin Sanchez-Lengeling,<sup>3,4,5</sup> Samuel M. Blau,<sup>\*6</sup> Gabe Gomes<sup>\*1,7,8</sup>

1. Department of Chemical Engineering, Carnegie Mellon University, Pittsburgh, PA 15213, USA
2. Department of Chemical Engineering, Federal University of Santa Maria, Santa Maria, RS, Brazil
3. Google DeepMind, Cambridge, MA, USA (*previous affiliation, where most of this work was done*)
4. Department of Chemical Engineering and Applied Chemistry, University of Toronto, Toronto, ON M5S 3E5, Canada (*current affiliation*)
5. Vector Institute for Artificial Intelligence, Toronto, ON, Canada (*current affiliation*)
6. Energy Technologies Area, Lawrence Berkeley National Laboratory, Berkeley, CA 94720, USA
7. Department of Chemistry, Carnegie Mellon University, Pittsburgh, PA 15213, USA
8. Wilton E. Scott Institute for Energy Innovation, Carnegie Mellon University, Pittsburgh, PA 15213, USA

\* corresponding authors: [smblau@lbl.gov](mailto:smblau@lbl.gov), [gabegomes@cmu.edu](mailto:gabegomes@cmu.edu)

## Table of Contents

<b>SIMG prediction model</b> .....	<b>2</b>
<b>General notes</b> .....	<b>2</b>
<b>evolver module</b> .....	<b>3</b>
Node reordering process.....	3
Permutation-invariant loss function.....	3
Examples of application.....	4
Results in comparison to other methods.....	5
<b>Active learning process</b> .....	<b>6</b>
<b>Baseline node embedding space</b> .....	<b>9</b>
<b>Protein SIMG* prediction performance</b> .....	<b>9</b>

# SIMG prediction model

## General notes

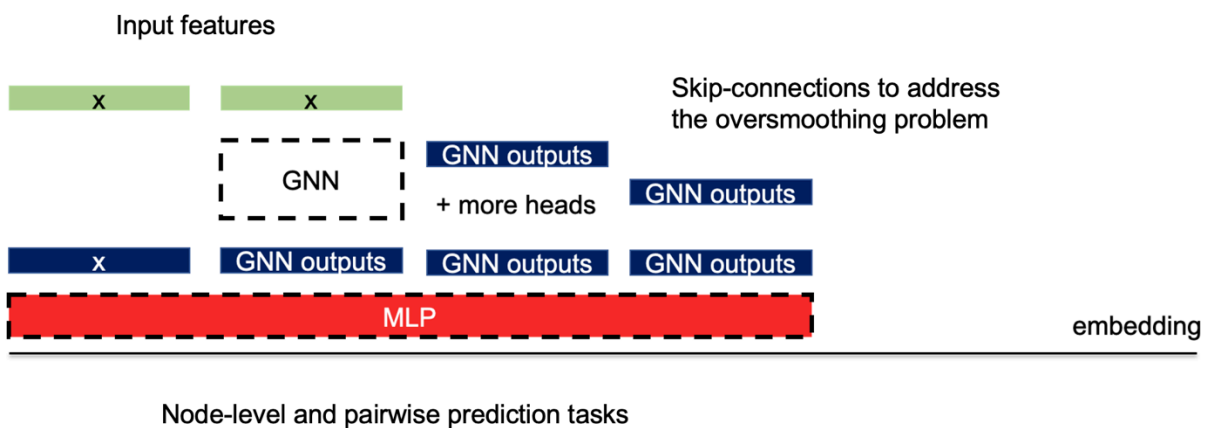


**Figure S1.** General overview of the architecture. Skip-connections were added to tackle over smoothing problem.

## evolver module

### Node reordering process

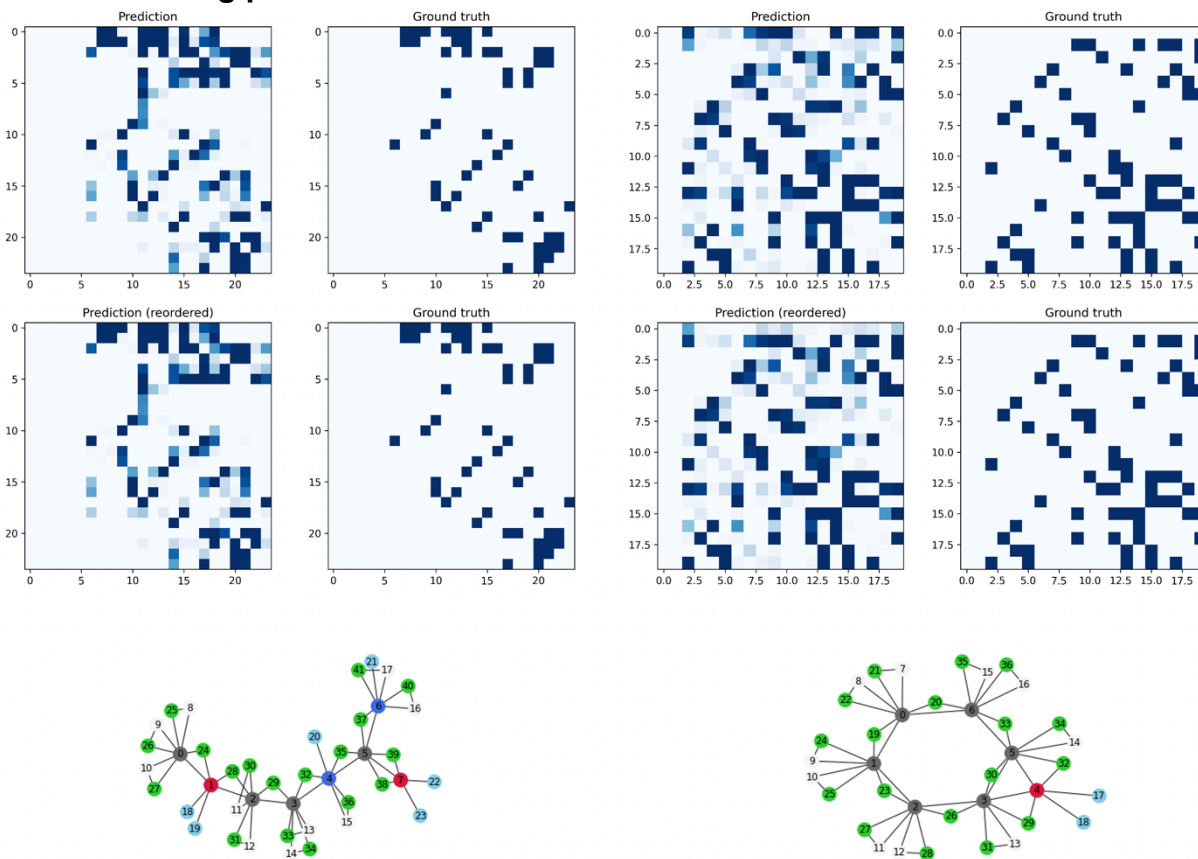


**Figure S2.** Overview of the node reordering procedure results for one of checkpoints for *evolver*-based model. Graphs below represent input extended molecular graphs.

### Permutation-invariant loss function

The `TotalLoss` class defines a custom loss function for a neural network model that processes graph structures, focusing particularly on preserving permutation invariance among node groupings. The class is structured to compute multiple types of losses: node loss via `NodeLoss`, link prediction loss via binary cross-entropy (`BCEWithLogitsLoss`), atom-to-bond loss via mean squared error (`MSELoss`), and interaction loss. One significant feature of `TotalLoss` is its optional node matching step, controlled by the `perform_matching` flag. If enabled, this step reorders nodes according to a matching obtained from the `get_matching` function, which ensures that the node predictions (`node_preds`) are aligned with the targets (`node_targets`) based on their similarity. This is critical for learning graph representations where the ordering of nodes within groups can vary but should not affect the model's outcome — hence ensuring permutation invariance. The remaining calculations adjust predictions

and target tensors for links and interactions based on these matchings, filtering out affected components to properly align paired elements before the final computation of the combined loss using the individual losses. This approach ensures that the loss computation respects the inherent permutation invariance required in many graph-based applications, making the model robust to node reorderings within identified groups of lone pairs.

### Examples of application

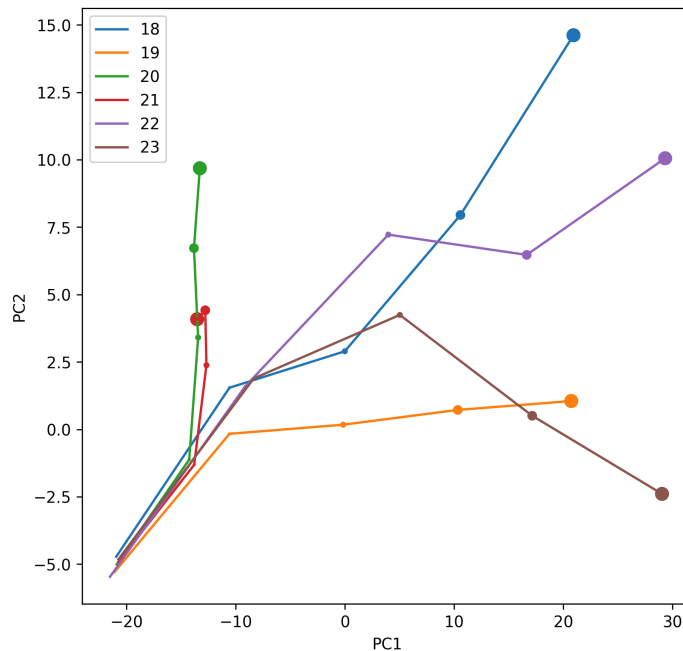


**Figure S3.** Example changes of lone positions in PCA space over multiple iterations. Point size indicates step.

## Results in comparison to other methods

$R^2$  score, lone pair *s*-character prediction

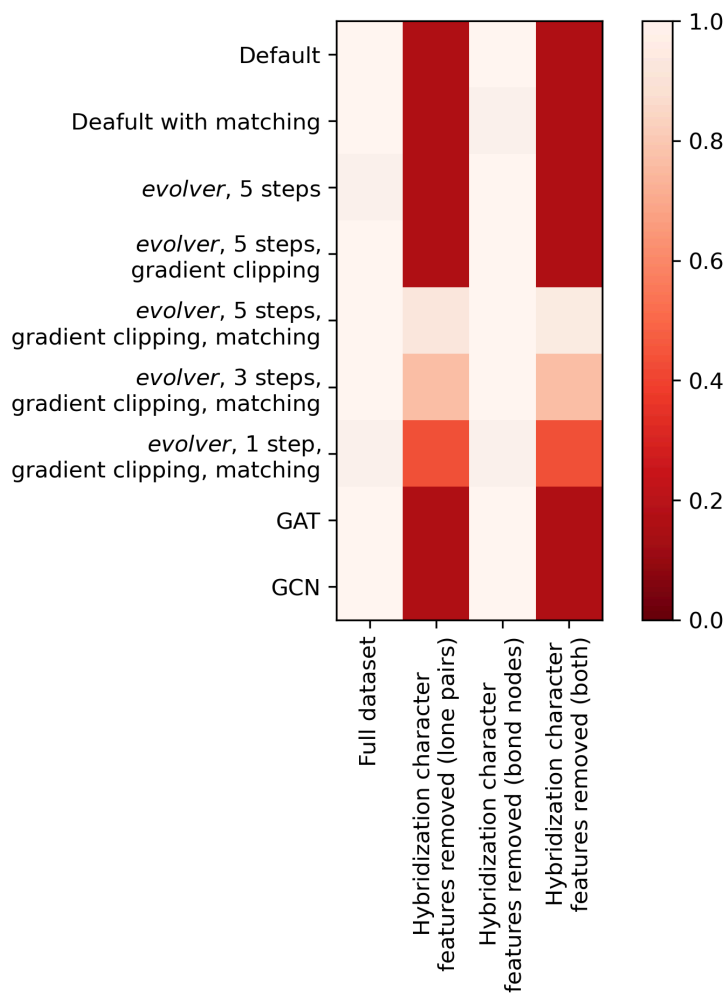


**Figure S4.** Results for lone pair prediction model (*s*-character)

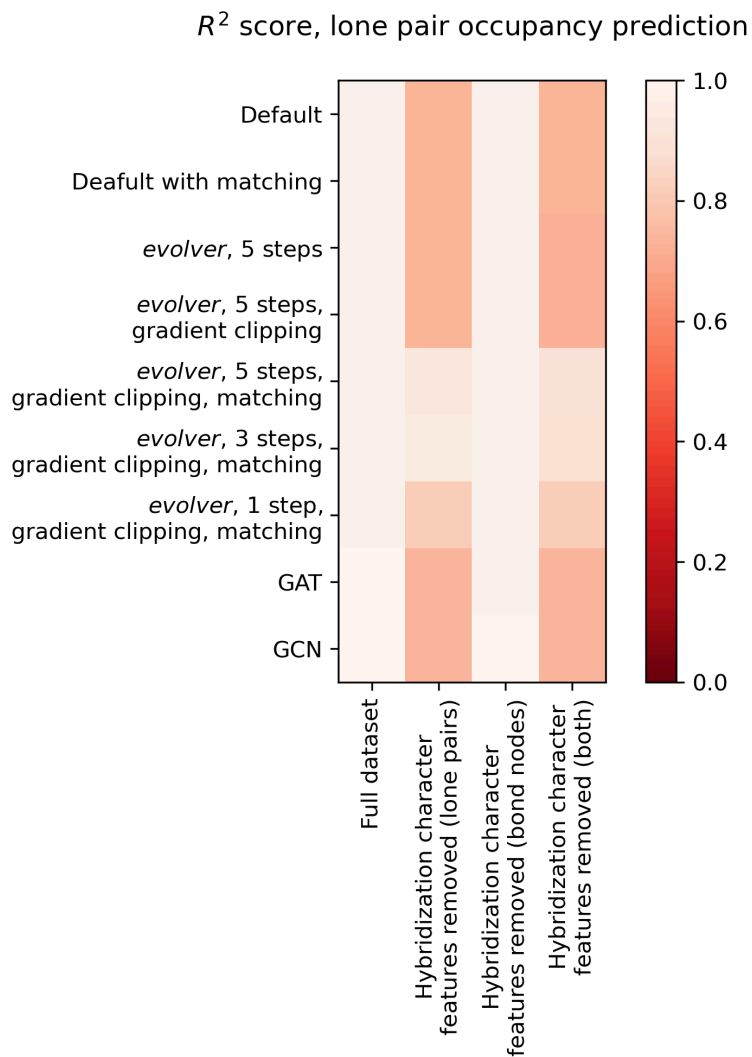


**Figure S5.** Results for lone pair prediction model (occupancy)

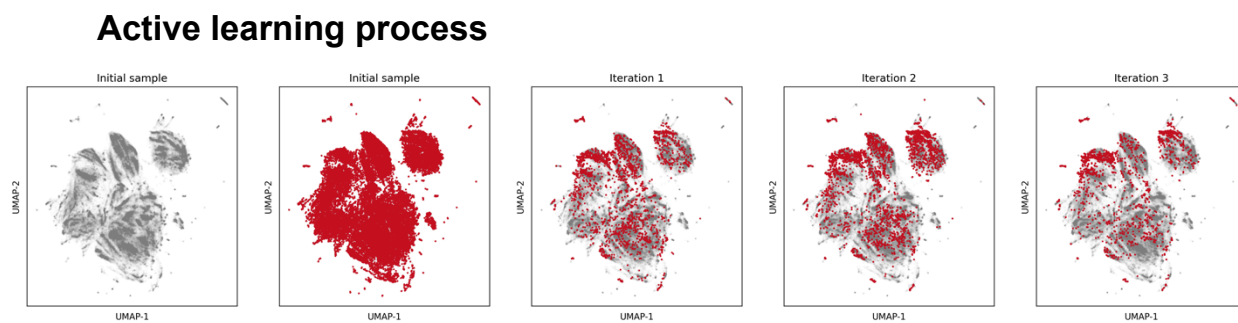


**Figure S6.** UMAP plot of chemical space navigation during active learning procedure.

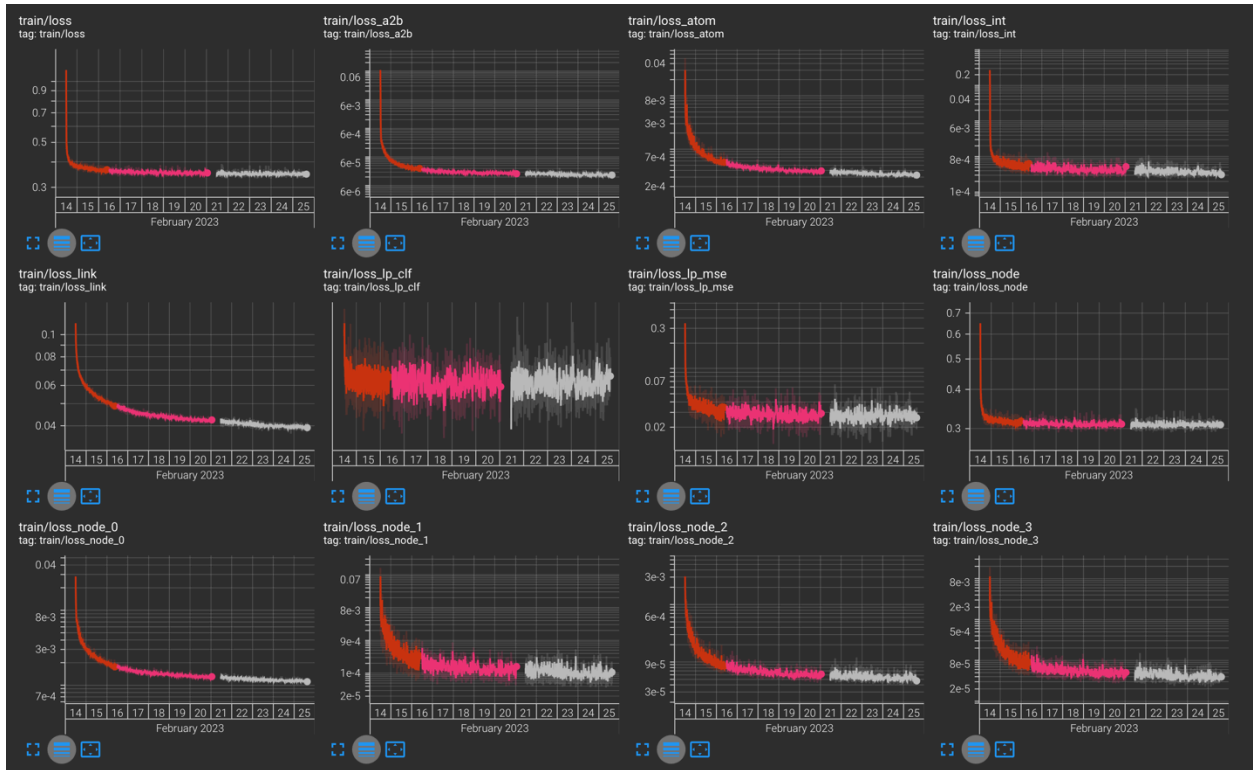
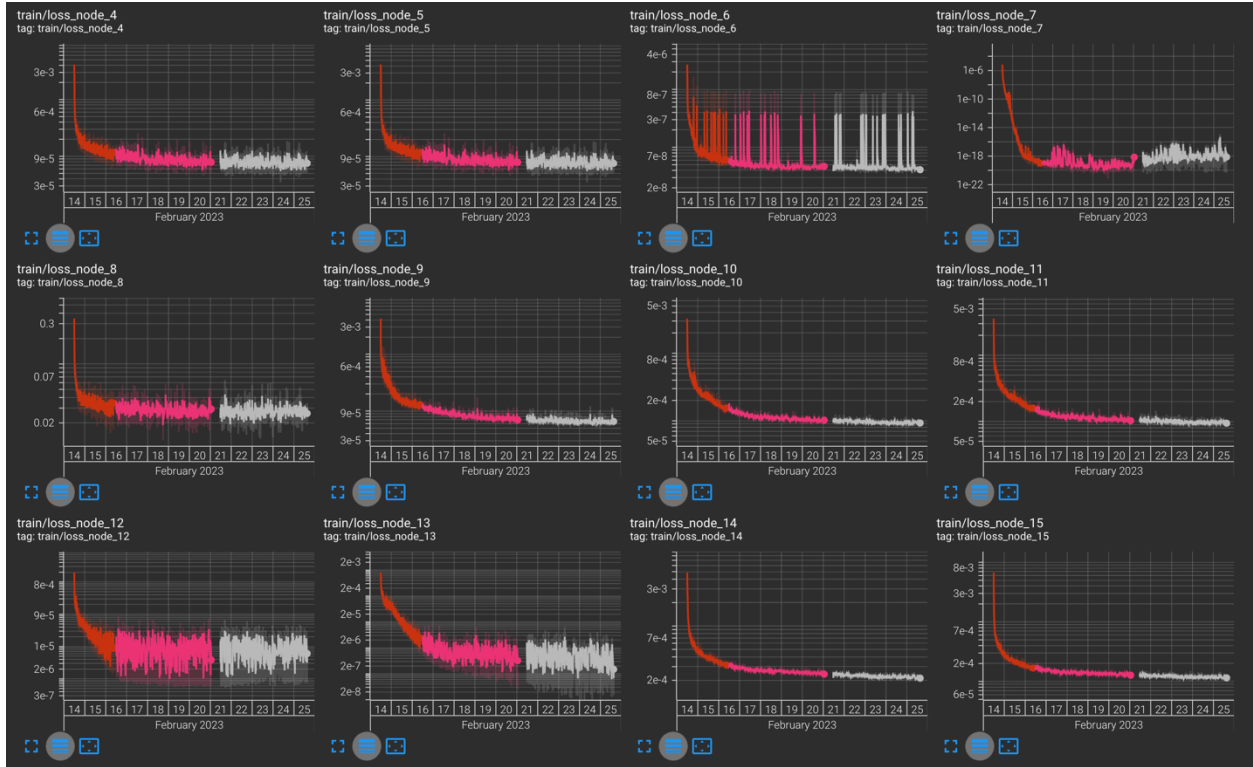


Figure S7. Training loss curves for the final model training run.

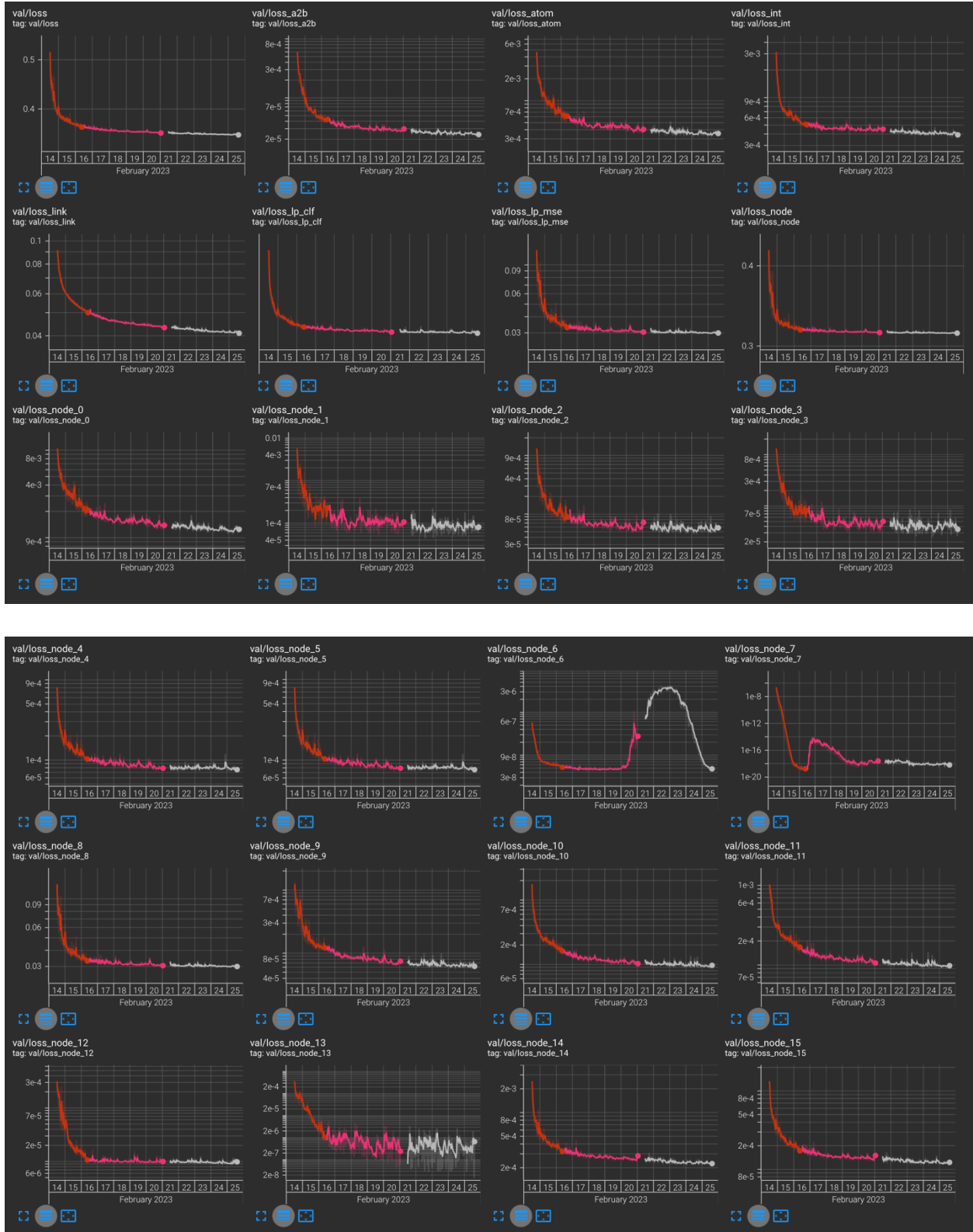
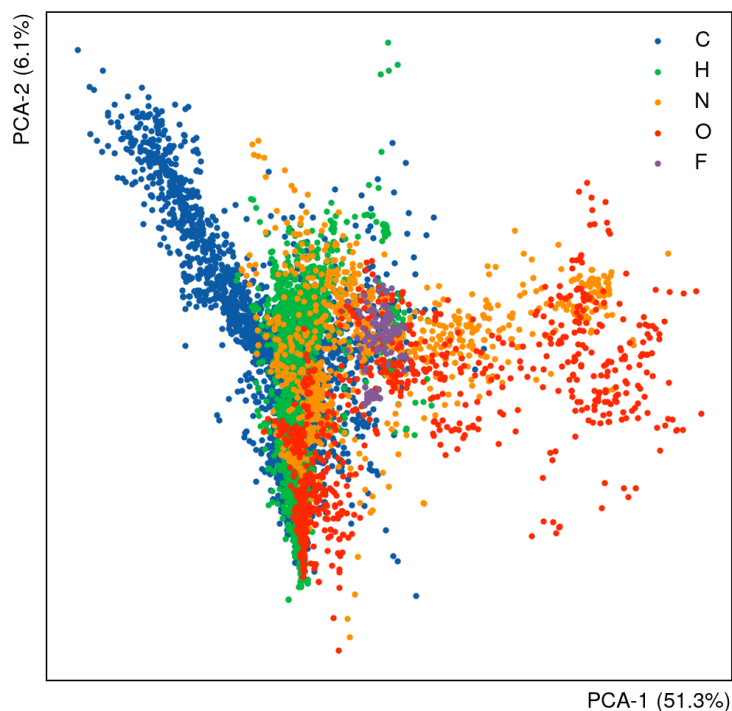


Figure S8. Validation loss curves for the final model training run.

## Baseline node embedding space

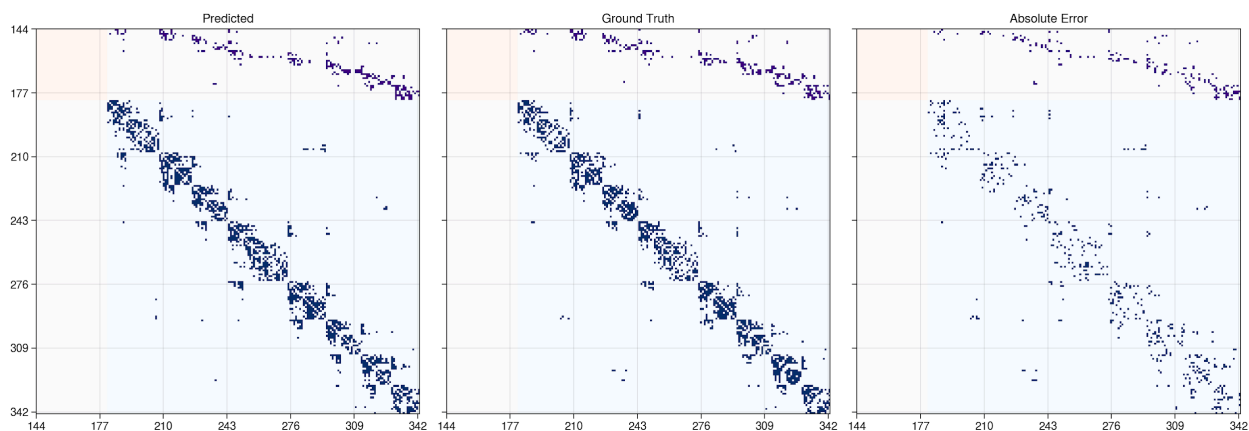


**Figure S9.** Node embedding space for GNN model, trained to predict QM9 targets.

## Protein SIMG\* prediction performance

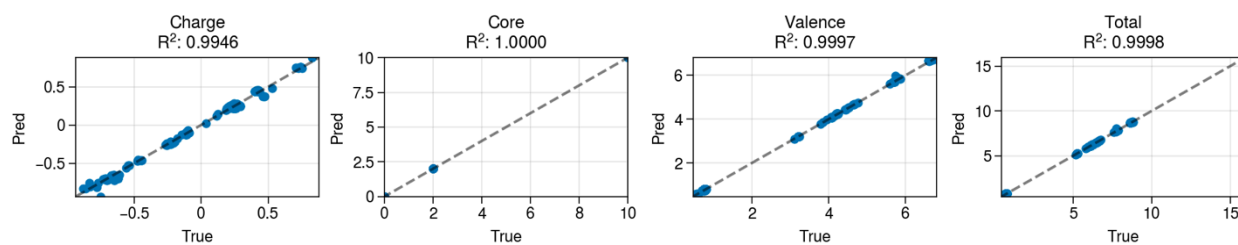
Interaction matrices depict the connections between orbital nodes in SIMGs, organized by their respective indices  $i$  and  $j$ . An entry of 1 at position  $(i, j)$  indicates an interaction where electron density is transferred from donor  $j$  to acceptor  $i$ . The indices are arranged such that lone-pair (LP) nodes precede bond nodes. Red areas in the matrix signify non-existent interactions between lone pairs of electrons. Purple areas denote interactions between bond orbitals and lone pairs, while blue areas illustrate interactions among bond orbitals.

Figure S10 displays the interaction matrices for both the predicted and ground-truth graphs, as well as their absolute differences, for the out-of-distribution protein with PDB code 1k4d. The model demonstrates high accuracy in predicting a large number of interactions and correctly identifies the absence of interactions between lone pairs or electron density transfer from bond orbitals to electron-rich lone-pair orbitals. The threshold used for these predictions was set at 0.95.



**Figure S10.** Predicted, ground-truth interactions matrices for protein PDB code 1k4d, followed by the absolute error.

Moreover, the model accurately predicts properties for this molecule. Proving that it is able to generalize to arbitrary long, out-of-distribution, molecules. Figure 11a, b, and c show predictions for node, lone-pair, and bond orbitals, respectively.



**Figure S11a.** Predicted atom node targets.

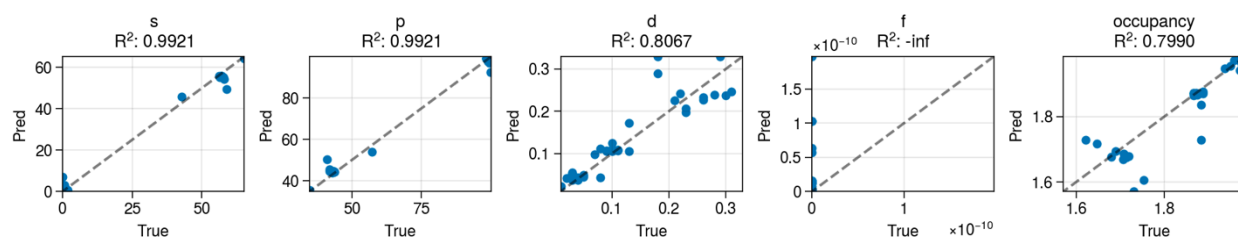


**Figure S11b.** Predicted lone-pair node targets.

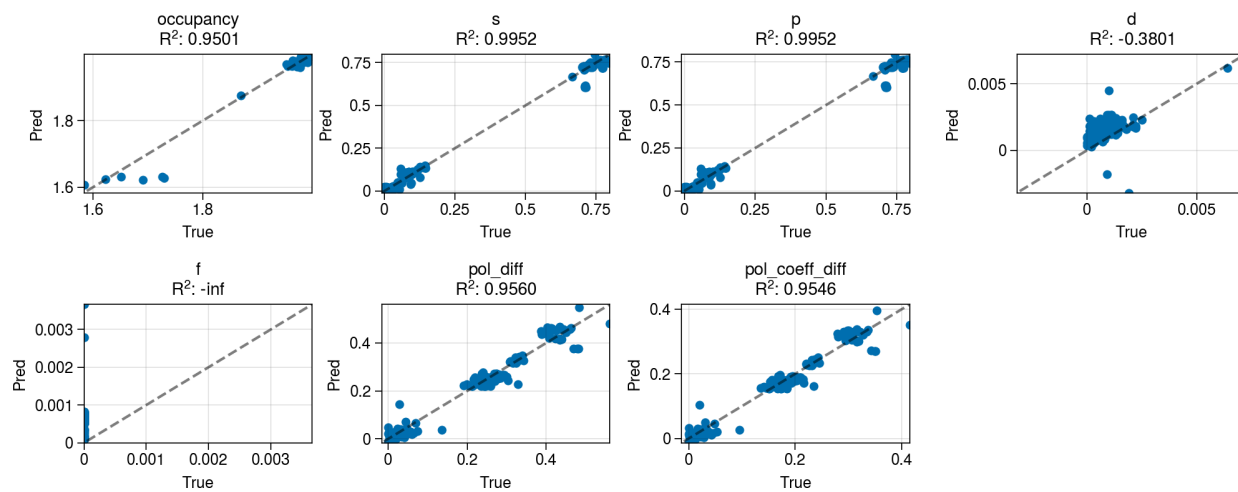


**Figure S11c.** Predicted bond orbital node targets.